

Density functional theory study of clean, hydrated, and defective alumina ($1\bar{1}02$) surfacesSara E. Mason,¹ Christopher R. Iceman,² Thomas P. Trainor,² and Anne M. Chaka¹¹*Physics Laboratory, National Institute of Standards and Technology, Gaithersburg, Maryland 20899, USA*²*Department of Chemistry and Biochemistry, University of Alaska Fairbanks, P.O. Box 756160, Fairbanks, Alaska 99775, USA*

(Received 16 December 2009; revised manuscript received 1 March 2010; published 19 March 2010; corrected 1 April 2010)

We report an *ab initio* thermodynamic analysis of the α -Al₂O₃ ($1\bar{1}02$) surface aimed at understanding the experimentally observed terminations over a range of surface preparation conditions as well as a stoichiometric model for the (2×1) surface reconstruction observed after high-temperature annealing. As temperature is increased under both ultrahigh vacuum and ambient hydrated conditions, the predicted minimum-energy structural model goes through the same series of changes: from the hydroxylated “missing-Al” surface model (or half-layer model in which the topmost Al site of the stoichiometric surface has zero occupancy), to the hydroxylated stoichiometric model, to another hydroxylated missing-Al surface model with tetrahedral coordinated surface Al, and finally to the clean (1×1) stoichiometric model. These results are in agreement with observations of both missing-Al and bulklike stoichiometries under wet conditions and in agreement with similar trends reported for isostructural hematite. However, we observe that the models with excess oxygen have a relatively higher surface-free energy and distinct surface relaxations in the case of alumina as compared to hematite. At very high temperatures where oxygen defects are generated, we find that a stoichiometric, charge-neutral (2×1) structure becomes the most thermodynamically stable. This is consistent with the observation of a (2×1) electron diffraction pattern when the surface is annealed at 2000 K while a (1×1) pattern persists at lower annealing temperatures. A general rule that emerges from our modeling results is that while the full phase space of hydrated and defective surfaces is expansive, model stoichiometries that can be made charge neutral through either hydration or defects offer the greatest thermodynamic stability. However, the unique trends in structure and relative energies of alumina surface stoichiometries as compared to hematite can be understood based on the difference in electronic structure of the substrate.

DOI: [10.1103/PhysRevB.81.125423](https://doi.org/10.1103/PhysRevB.81.125423)

PACS number(s): 68.47.Gh, 68.43.Bc, 68.35.Md

I. INTRODUCTION

Within the past decade, considerable effort has been devoted to understanding how metal-oxide surface structures vary from ultrahigh vacuum (UHV) conditions to fully hydrated conditions (e.g. Refs. 1–13). As surface structure, polarity, and hydration significantly affect reactivity, understanding how these properties vary with changes in environmental or operational conditions is essential to understanding reactions at metal-oxide-water interfaces. Such interfacial reactions play a major role in a variety of environmental and technological applications such as contaminant remediation,¹⁴ catalysis for automotive pollution control,¹⁵ solid oxide fuel cells,¹⁶ and nanoscale biosensors.¹⁷ Understanding of the unique (compared to UHV conditions) structure-property relationships exhibited by metal-oxide interfaces requires accurate structural models and motivates our study of the hydrated α -Al₂O₃ ($1\bar{1}02$) surface.

A. Bulk and UHV Al₂O₃

Bulk α -Al₂O₃ belongs to the $R\bar{3}c$ space group and the structure consists of alternating planes of O and Al atoms running perpendicular to the (0001) direction. The Al layers are hexagonally arranged with Al occupying 2/3 of the available octahedral sites. Electrostatic repulsion results in two sublayers of Al between oxygen double layers.¹⁸

The ($1\bar{1}02$) surface exhibits a rectangular (1×1) unit cell indexed by \mathbf{a}_s defined by the $[110]$ bulk lattice vector and \mathbf{b}_s

defined by the $[\frac{1}{3}\frac{1}{3}\frac{1}{3}]$ bulk lattice vector.¹⁹ Under UHV conditions, low-energy electron-diffraction and Auger-electron spectroscopy studies report the annealed ($1\bar{1}02$) surface to be extremely clean, chemically stable, and well ordered.²⁰ Reflection high-energy electron-diffraction (RHEED) and atomic-force-microscopy experiments of the clean α -Al₂O₃ surface report that both a (1×1) surface (after annealing at 1100 K) and (2×1) surface reconstruction pattern (attributed to ordered oxygen vacancies after annealing at 2000 K) are observed.^{21,22} Unlike the 0 K UHV preferred Al termination found on the clean (0001) surface,²³ the minimum energy 0 K UHV clean ($1\bar{1}02$) surface is predicted by density-functional-theory calculations of Guo *et al.*²⁴ to be terminated by an O layer. However, the terminations observed under UHV may not persist under non-UHV conditions, particularly in the presence of water.

B. Measurements of hydroxylated surface structures

When immersed in aqueous solutions, metal-oxide surfaces are expected to hydroxylate via the dissociative chemisorption of water molecules.²⁵ This change in the stable surface termination under hydrating conditions has been studied extensively on the (0001) alumina surface through both experimental^{26–28} and theoretical methods.^{29–32} Whereas under UHV conditions the Al-terminated (0001) surface is found to be the most stable under UHV conditions, a fully hydroxylated, oxygen-terminated surface is found to be

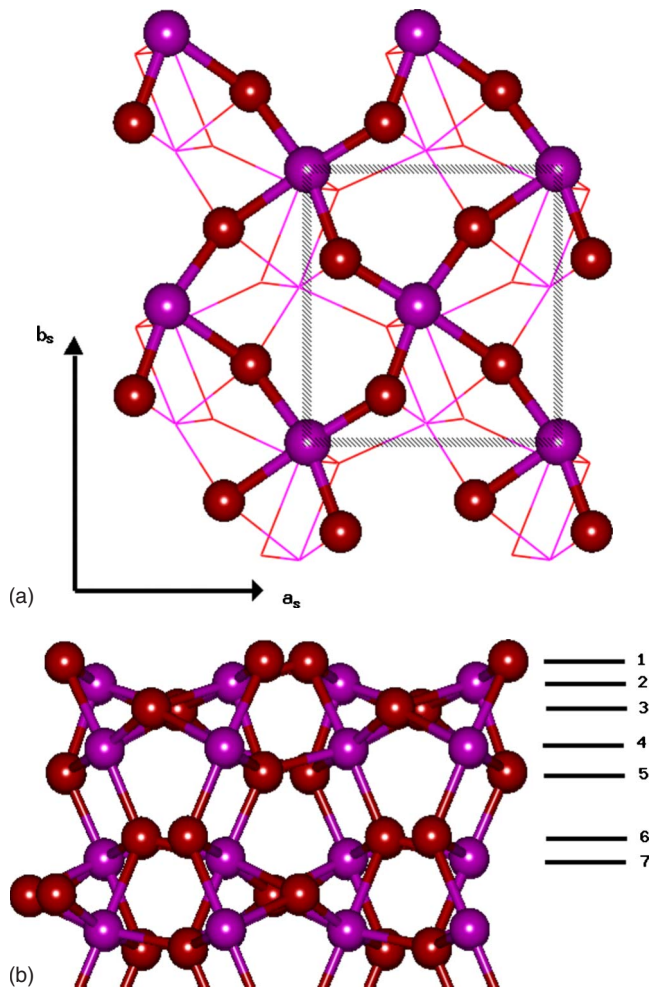


FIG. 1. (Color online) Model of the stoichiometric bulk termination of Al_2O_3 ($1\bar{1}02$). Oxygen atoms are shown in red and Al atoms are in magenta. (a) Top-view showing the surface net. The first layer O, second layer Al, and third layer O are shown in a ball-and-stick representation while the layer 4-7 Al and O atoms are shown in a line representation. The (1×1) unit cell is indicated by the dashed rectangle. The real-space vector directions are indicated. (b) Side-view showing the layer stacking sequence.

stable under a wide range of finite pressure and temperature conditions.

The hydrated $\alpha\text{-Al}_2\text{O}_3$ ($1\bar{1}02$) surface structure differs substantially from the (0001) hydrated surface, exhibiting different terminal oxygen coordination chemistry and therefore different reactivity.³³ Top and side views of the stoichiometric surface are shown in Figs. 1(a) and 1(b). Two different surface structures have been proposed under hydrating or hydrous conditions.^{19,34} A surface scattering study of the hydrated $\alpha\text{-Al}_2\text{O}_3$ ($1\bar{1}02$) surface concluded that the dominant termination is a “missing-Al” model, in which the fivefold coordinated Al atoms of the stoichiometric surface have been lost.¹⁹ This surface structure is also referred to as the half-layer or “Al-vacancy” model because the surface termination is deficient by a layer of Al relative to a bulk continuation. As noted in Ref. 35, the resulting channeled structure in the missing-Al model resembles a face-centered-cubic (110) sur-

face topography. While protons positions are not observed in the x-ray scattering study, it is expected that the surface charge is balanced by the replacing each lost Al^{3+} with the addition of 3 H^+ , leading to a charge-neutral hydroxylated surface. In contrast, Catalano *et al.*³⁴ reported a hydrated stoichiometric termination, in which an additional oxygen (or hydroxyl) layer coordinates the surface aluminum, dominates under hydrous conditions.

In this study we investigate how the discrepancy between the observations is likely tied to the different surface conditions employed in experimental studies. Trainor *et al.* prepared the surface under UHV conditions using Ar^+ sputtering and oxygen annealing to approximately 1200 K followed by dosing with H_2O in a UHV chamber. Catalano *et al.* prepared their sample by low-temperature annealing (about 650 K) in air and subsequently hydroxylated the surface by contact with aqueous solutions. As observed in the analogous $\alpha\text{-Fe}_2\text{O}_3$ ($1\bar{1}02$) surface system,^{9,36,37} the observation of stoichiometric and missing-Fe structural models was shown experimentally to be a result of surface preparation.³⁸ These experimental observations were explained by the theoretical work of Lo *et al.*³⁷ who found a crossover in the surface stability with temperature. Furthermore, recent atomic-force-microscopy experiments on Al_2O_3 surfaces demonstrated that on the ($1\bar{1}02$) surface, the average step height and terrace width show a much stronger dependence on annealing temperature than on the (0001) surface,³⁹ further demonstrating how preparation conditions influence surface morphology of this termination.

In this work, we use first-principles modeling to study different stoichiometries and protonation states of clean, hydrated, and defective (by ordered oxygen vacancies) $\alpha\text{-Al}_2\text{O}_3$ ($1\bar{1}02$) surfaces. Our results provide a basis for understanding the variations in surface stoichiometry observed under different surface preparation conditions. Our study builds upon previous theoretical work^{24,40,41} by considering a wider range of terminations and stoichiometries and focusing on understanding the different experimentally observed terminations over a range of pressure and temperature conditions. The hydrated models investigated here are analogous to those proposed and studied by Lo *et al.*³⁷ for the isostructural $\alpha\text{-Fe}_2\text{O}_3$ ($1\bar{1}02$) surface. We present a detailed *ab initio* investigation of these surfaces in terms of structure and thermodynamic stability under a range of experimentally relevant temperature and pressure conditions.

II. METHODOLOGY AND COMPUTATIONAL DETAILS

Periodic density-functional-theory (DFT) calculations are carried out with the Perdew, Burke, and Ernzerhof (PBE) generalized gradient approximation (GGA) to the exchange-correlation functional.⁴² All-electron calculations are performed using a double-numeric-plus-polarization, atom-centered basis set as implemented in the DMol³ code.^{43–45} Bulk lattice optimizations are converged with respect to k points using a $(5 \times 5 \times 5)$ Monkhorst-Pack grid⁴⁶ to sample the Brillouin zone, and a 4.5 Å real space cutoff (r_{cut}). In surface calculations, r_{cut} is reduced to 3.5 Å, which has been

previously reported to only minimally affected resulting calculated surface-free energies on hematite.^{37,47} We further test the reduction in r_{cut} on the alumina surface by considering the range of r_{cut} from 3.5 to 5.0 Å in 0.5 Å increments. The resulting calculated surface-free energies (as defined below) vary by less than 5 meV/Å², within reason for the desired accuracy in the *ab initio* thermodynamic model.⁴⁸ The optimized bulk lattice constants of 4.823 Å(+1.3%) and 13.111 Å(+0.9%) for $\alpha\text{-Al}_2\text{O}_3$ are in excellent agreement with experiment (differences from experiment are indicated in parentheses)⁴⁹ and other GGA results.^{10,18,30,50,51}

The $\alpha\text{-Al}_2\text{O}_3$ (1 $\bar{1}$ 02) surfaces are modeled using (1×1) periodic cells of 16–22 atomic layers depending on surface stoichiometry. Our theoretical in-plane lattice parameters of $\mathbf{a}_s=4.825$ Å and $\mathbf{b}_s=5.200$ Å are in good agreement with the experimental values of 4.757 Å and 5.127 Å for \mathbf{a}_s and \mathbf{b}_s , respectively.¹⁹ Top and side views of the stoichiometric surface and the (1×1) unit cell are shown in Figs. 1(a) and 1(b). Periodic images along the surface normal are separated by at least 10 Å of vacuum. The top and bottom surfaces are related by inversion symmetry, and full geometry optimization is carried out on the entire slab with a structural convergence set to a force tolerance of 0.01 eV/Å. The slab is of sufficient thickness such that the central layers exhibit bulk-like geometry without imposed constraints. A converged (5×5×1) Monkhorst-Pack k -point grid⁴⁶ is used for the surface calculations. Surfaces with ordered oxygen vacancies are modeled in (2×1) periodic cells with a (5×2×1) k -point grid.

Vibrational frequencies are determined within DMol³ employing a frozen phonon method⁵² using two displacements per atom (of step size 0.01 a_0) to construct the mass-weighted Hessian matrix. Subsequent diagonalization yields the harmonic frequencies of the slab. In all cases, full Hessian matrix calculations are carried out.

The small molecules O₂, H₂, and H₂O are modeled in the same (1×1) periodic cell as the $\alpha\text{-Al}_2\text{O}_3$ (1 $\bar{1}$ 02) surface and using identical computational methods and parameters. While these methods are not optimized for calculating small molecule properties, our goal is to treat all species involved in the thermodynamic analysis (bulk, slabs, and molecules) with the same level of theory for consistency and optimal error cancellation in computed differences.

A. *Ab initio* thermodynamics

The goal of the *ab initio* thermodynamic analysis applied here is to predict the relative stability of chemically distinct surface terminations under variable environmental conditions, including variable temperature, and oxygen, hydrogen, and water partial pressures. The Gibbs free energy, defined as $G=H-TS$, where H is the enthalpy and S is the entropy, is the governing thermodynamic state function under conditions of fixed temperature T and pressure p . The equilibrium between the substrate and a gas phase is constrained at conditions of constant T and p such that the chemical potential of a given chemical component (μ_i) is equivalent in all phases present in the system. The surface-free energy $\gamma(T,p)$, is defined as

$$\gamma(T,p,N_i) = \frac{1}{2A} \left\{ G_{\text{slab}}(T,p,N_i) - \sum_i N_i \mu_i(T,p) \right\}, \quad (1)$$

where G_{slab} is the calculated Gibbs free energy of the solid slab, N_i is the number of the i th type of atom, and A is the surface area. The factor of $(2A)^{-1}$ normalizes $\gamma(T,p,N_i)$ to energy per unit area for a semi-infinite slab with two equivalent surfaces.

In applying Eq. (1), it is important to consider how to relate DFT total energies to the appropriate thermodynamic quantities and correct for DFT errors where necessary. The total energy from DFT calculations, done at constant volume and composition, provides the 0 K enthalpy ($H=U+pV$, where U is the internal energy) but does not include any vibrational contributions. Connecting DFT total energies to thermodynamics requires accounting for the vibrational energy (including zero-point energy) and the entropy. Previous work by Reuter and co-workers⁴⁸ found that for a desired ± 10 meV/Å² accuracy in systems not including hydrogen, both vibrational and entropic contributions cancel out in taking the differences between surface and bulk terms in Eq. (1), and the pV contribution to the surface-free energy is also negligible. However, as noted in later work,⁵³ the entropy contributions from adsorbed hydroxyl and waterlike species to the surface-free energy have no counterpart in the bulk, and must be accounted for in order to maximize agreement with experiment. The main contribution to the entropy of adsorbed water and water dissociation products is the vibrational entropy contribution to the free energy, ΔG^{vib} (set to zero at 0 K). We include this term in the surface Gibbs free energy by calculating the vibrational partition function of the full slab

$$q_v = \prod_i^{N_m} \frac{e^{-\beta h \nu_i / 2}}{1 - e^{-\beta h \nu_i}}, \quad (2)$$

where N_m is the number of vibrational modes and β is defined in terms of the Boltzmann constant k_B as $1/k_B T$. The vibrational energy is related to q_v by $E^{\text{vib}} = -\frac{\delta}{\delta \beta} \ln q_v$ and the vibrational entropy is given by $S^{\text{vib}} = k(\ln q_v + \beta E^{\text{vib}})$. Using the definition of the vibrational temperature ($\Theta_{v_i} = h \nu_i / k_B$) gives

$$\Delta G^{\text{vib}} = k_B \sum_i \Theta_{v_i} \left(\frac{1}{2} + \frac{1}{e^{\Theta_{v_i}/T} - 1} \right) - k_B T \sum_i \left[\frac{\Theta_{v_i}/T}{e^{\Theta_{v_i}/T} - 1} - \ln(1 - e^{-\Theta_{v_i}/T}) \right]. \quad (3)$$

As each surface is considered here to be in chemical and thermal equilibrium with the bulk and the gas phase, the chemical potentials of each type of atom must be equal in all phases. The physical constraints on the ranges of μ_O , temperature and pressure dependence, and equilibrium with other species, within this type of analysis have been detailed previously,^{30,48,53,54} and are stated here explicitly for our model systems. We also carefully assess and, as necessary, correct for sources of DFT error.

The range of μ_{O} at our chosen reference state (0 K) is defined by considering the limiting behavior at oxygen-rich and oxygen-poor extremes and using an appropriate choice of theoretical or experimental standard values. At the oxygen-rich limit, gas-phase oxygen condenses at the surface. At the oxygen-poor limit, the oxide surface decomposes into solid bulk aluminum and gas-phase O_2 . As done in previous studies on similar surfaces,^{30,37} we approximate the limiting values of μ_i by defining them in terms of DFT total energies. Therefore, we define

$$\mu_{\text{O,max}} = \frac{1}{2}E_{\text{O}_2}, \quad (4)$$

where E_{O_2} is the total energy of the O_2 molecule. We rescale $\mu_{\text{O,max}}$ to zero in phase diagrams while using the explicit value in computing surface-free energies. The minimum 0 K oxygen chemical potential is defined by

$$\mu_{\text{O,min}} = \frac{1}{3}E_{\text{Al}_2\text{O}_3,\text{bulk}} - \frac{2}{3}E_{\text{Al,bulk}}, \quad (5)$$

where the total energy used for bulk Al_2O_3 is for a single Al_2O_3 unit and the coefficients are derived from the balanced reaction $2\text{Al}_2\text{O}_3 = 4\text{Al} + 3\text{O}_2$ solving for μ_{O} per oxygen atom.

Values of μ_{H} are determined by the equilibrium between H_2 and H_2O in the gas phase within the limits of accessible μ_{O} . With respect to equilibrium with H_2 at 0 K, the hydrogen chemical potential is

$$\mu_{\text{H}} = \frac{1}{2}E_{\text{H}_2,\text{gas}} \quad (6)$$

or with respect to equilibrium with H_2O , the 0 K hydrogen chemical potential is defined as

$$\mu_{\text{H}} = \frac{1}{2}(E_{\text{H}_2\text{O,gas}} - \mu_{\text{O}}). \quad (7)$$

As discussed in Ref. 48, the temperature and pressure dependence of $\mu(T, p)$ for gas phase species at a pressure p^o can be calculated using

$$\mu_i(T, p) = \mu_i(T, p^o) + \frac{1}{2}kT \ln\left(\frac{p}{p^o}\right). \quad (8)$$

We use the NIST-JANAF tables⁵⁵ to determine the temperature dependence of the gas phase species at standard pressure and Eq. (8) to compute the chemical potentials at the desired pressures. For the bulk oxide, we use the NIST-JANAF tables⁵⁵ for the enthalpic and entropic contributions to $\mu_{\text{Al}_2\text{O}_3}$.

Finally, we write out Eq. (1) explicitly for our system. In doing so, we use the fact that all of the species are in equilibrium with each other, which allows us to relate their chemical potentials. Specifically, $2\mu_{\text{Al}} + 3\mu_{\text{O}} = G_{\text{Al}_2\text{O}_3}^{\text{bulk}}$, $\mu_{\text{H}_2\text{O}} = 2\mu_{\text{H}} + \mu_{\text{O}}$, and $\mu_{\text{O}} = \frac{1}{2}G_{\text{O}_2}^{\text{gas}} = \frac{1}{2}\mu_{\text{O}_2}$. Therefore

$$N_{\text{Al}}\mu_{\text{Al}} = \frac{1}{2}N_{\text{Al}}G_{\text{Al}_2\text{O}_3}^{\text{bulk}} - \frac{3}{2}N_{\text{Al}}\mu_{\text{O}},$$

$$N_{\text{H}}\mu_{\text{H}} = \frac{1}{2}N_{\text{H}}\mu_{\text{H}_2\text{O}} - \frac{1}{2}N_{\text{H}}\mu_{\text{O}} \quad (9)$$

and

$$\begin{aligned} \gamma(T, p, N_i) = & \frac{1}{2A} \left[E_{\text{slab},0 \text{ K}} + \Delta G^{\text{vib}} - \frac{1}{2}N_{\text{Al}}\mu_{\text{Al}_2\text{O}_3(T,p)} \right. \\ & \left. + \left(\frac{3}{2}N_{\text{Al}} - N_{\text{O}} \right) \mu_{\text{O}} - N_{\text{H}}\mu_{\text{H}} \right]. \quad (10) \end{aligned}$$

It should be noted that the only independent variables in our *ab initio* thermodynamic analysis are μ_{O} in equilibrium with bulk Al_2O_3 , and μ_{H} . The chemical potentials of the remaining species considered in the relevant equilibria (Al , O_2 , H_2 , and H_2O) are dependent. In practice, meaningful application of the above outlined method requires careful consideration of theoretical errors and physical limits.

An important practical consideration in applying the above model is the use of either calculated or experimental values in defining the values and ranges of μ_i . When comparing total energy differences for diverse species such as three-dimensional periodic solids, two-dimensional periodic slabs of finite thickness, and small molecules such as H_2 and spin-polarized O_2 , it is essential to understand the magnitude of errors inherent in the methodology for each species and to minimize or compensate for them where possible. Convergence of computed bulk and surface properties is discussed above, and is standard in DFT practice and established to be in good agreement with experiment. However, the triplet ground state and short bond distance of O_2 pose sources of theoretical error not found in the other species being compared in the thermodynamic model given by Eq. (10). The GGA-PBE error of the atomization energy per O_2 molecule [with zero-point energy (ZPE) removed for direct comparison with DFT values and using the same basis set, unit cell, and r_{cut} discussed in section II] using DMol³ is 0.90 eV; similar to the 1.00 eV value reported using another DFT implementation.⁴² A key question is if this inherent error is unique to the O_2 molecule (and thus necessitating a scheme for correction to E_{O_2}) or if it is a systematic error associated with all oxygen-containing species and hence will cancel when computing differences.

A good assessment of whether the known error in the DFT value for E_{O_2} fortuitously cancels out with error in the DFT value for $E_{\text{Al}_2\text{O}_3}$ is to determine the 0 K Gibbs free energy of formation for the oxide⁴⁸

$$\Delta G_f(T, p) = g_{\text{Al}_2\text{O}_3}^{\text{bulk}} - 2g_{\text{Al}}^{\text{bulk}}(T, p) - \frac{3}{2}g_{\text{O}_2}^{\text{gas}}(T, p), \quad (11)$$

where $g_{\text{Al}_2\text{O}_3}^{\text{bulk}}$, $g_{\text{Al}}^{\text{bulk}}$, and $g_{\text{O}_2}^{\text{gas}}$ are the Gibbs free energy of bulk Al_2O_3 , face-centered cubic bulk metallic Al, and isolated molecular oxygen, respectively, and lower case g is henceforth used to denote a Gibbs free energy per formula unit. At 0 K, we use our DFT-GGA total energies for the Gibbs free energy of each species in Eq. (11). Our DFT result for ΔG_f (0 K) recovers only 87% of the experimental value of 17.24 eV.⁵⁶ By adding a 0.90 eV correction (E^{corr} , determined from the DMol³ error in the atomization energy per O_2 molecule

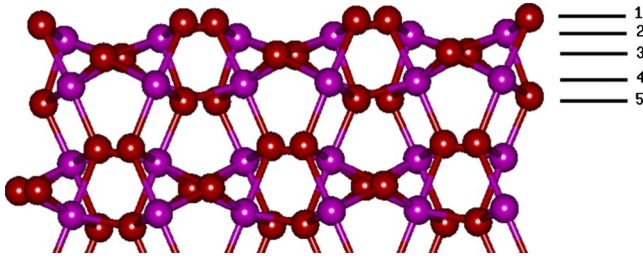


FIG. 2. (Color online) The A1 model for the α -Al₂O₃ ($1\bar{1}02$) surface with stoichiometry O₂-Al₂-O₂-Al₂-O₂-R. Three repeats of our (1 × 1) unit cell in the y direction are shown. Oxygen atoms are shown in red, aluminum atoms are in magenta, and hydrogen atoms (where present) are shown as gray spheres.

discussed above) to our DFT value of E_{O_2} , our DFT-GGA value for ΔG_f (0 K) α -Al₂O₃ reduces from -12.4% to -4.6%, indicating that the majority of the error is associated with the theoretical treatment of O₂. The magnitude of E^{corr} is dependent on the DFT implementation used, and as noted in other studies, is not always necessary.⁴⁸ However, this must always be carefully tested for. Otherwise, the error that propagates through the *ab initio* thermodynamics will potentially result in large magnitude temperature and pressure errors.⁵⁷ Here, neglecting the error in E_{O_2} does not affect which structural models are calculated to be stable but it does impact the pressure and temperature ranges over which stability is predicted. This leads to difficulties when comparing *ab initio* thermodynamics and experimental results as commented upon in other work.⁵⁷

Alternative to using our suggested E^{corr} to account for DFT error in E_{O_2} , the choice of functional and basis set can be adjusted to achieve a higher level of accuracy in the DFT description of O₂. However, the necessity to use consistent theoretical methods of all species in equilibrium (gas phase molecules, bulk oxide, and surface slabs) would be computationally prohibitive in the present study.

To assess the possible error introduced into the thermodynamic analysis by using DFT total energies for H₂ or H₂O, we again determine the theoretical atomization energies. The GGA-PBE error of the atomization energies per molecule of H₂ and H₂O (ZPE removed for direct comparison with DFT values) using DMol³ are 4.59 and 10.06 eV, respectively, again in good agreement with other DFT results.⁴² The magnitude of error between the ZPE-corrected experimental values⁴² and the present DFT values of -0.13 and 0.371 eV for H₂ and H₂O, respectively, are much smaller than the 0.9 eV error in the O₂ value.

To evaluate how the errors in H₂ and H₂O energies propagate through the *ab initio* thermodynamic model and affect the results, we return to the calculation of μ_H [Eq. (6) or Eq. (7)]. The appropriate equilibrium depends on whether oxygen-rich or oxygen-poor limits are considered. The accessible range of μ_O (as discussed above) is determined to be 5.48 eV. At a given set of conditions, the thermodynamically most stable system minimizes $\gamma(T, p)$ through thermal equilibrium with the gas phases. Therefore, as can be seen in Eq. (1), the appropriate equilibrium is the one that also minimizes μ_H . When hydrogen on the surface is in equilibrium

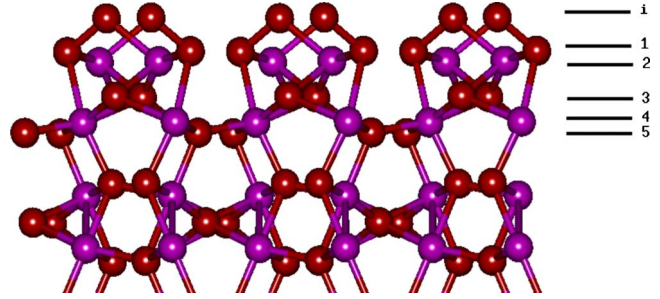


FIG. 3. (Color online) Same as Fig. 2 for A2: O₂-O₂-Al₂-O₂-Al₂-O₂-R.

with H₂, μ_H is equal to $\frac{1}{2}E_{H_2}$ [Eq. (6)] and independent of μ_O . When surface hydrogen is considered to be in equilibrium with H₂O, μ_H is determined by Eq. (7) with our DFT value of E_{H_2O} over the determined range μ_O . The result is that at 0 K, there is a crossover between μ_{H/H_2} and μ_{H/H_2O} within the range of μ_O such that for oxygen-poor conditions ($\mu_O < -2.88$ eV), the equilibrium with H₂ is appropriate for the determination of μ_H . For oxygen-rich conditions ($\mu_O > -2.88$ eV), the equilibrium with H₂ is appropriate for the determination of μ_H .

As we are chiefly concerned with the oxygen-rich limits in the present study, we need to assess to what extent our calculated surface-free energies $\gamma(T, p)$ are affected by the DFT error in E_{H_2O} . This quantity enters into the calculation of $\gamma(T, p)$ through μ_H as calculated using Eq. (7). Therefore, only surface models with nonzero hydrogen stoichiometries are affected. As there is no convenient test to determine if, or to what extent, DFT error in E_{H_2O} persists after the difference calculation of $\gamma(T, p)$, we analyze the impact assuming zero cancellation. For hydrated surface models, values of $\gamma(0$ K) are shifted by -15 to -44 meV/Å², depending on hydrogen content, when E_{H_2O} is corrected to reproduce the experimental atomization energy. Due to the sign of the error in the DFT H₂O atomization energy, the values of $\gamma(T, p)$ for hydrated surfaces using the uncorrected value of E_{H_2O} are less stable relative to the unaffected clean, hydrogen-free surfaces than if an H₂O E^{corr} is applied. As we cannot easily determine the persistence of the E_{H_2O} after subtracting total energies in Eq. (1), and as the magnitude is small, and as the direction of this error can only underestimate relative hydrated surface stability, we decide to use our uncorrected value of E_{H_2O} in the thermodynamic analysis.

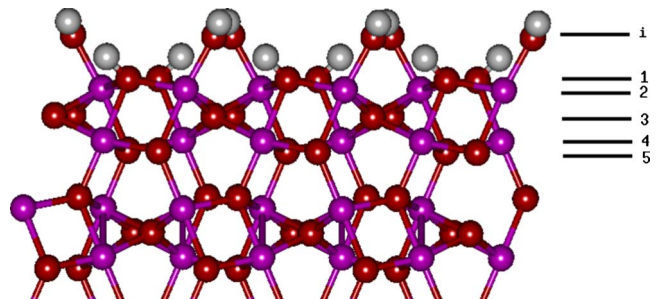


FIG. 4. (Color online) Same as Fig. 2 for A3: (HO)₂-O₂-Al₂-O₂-Al₂-O₂-R.

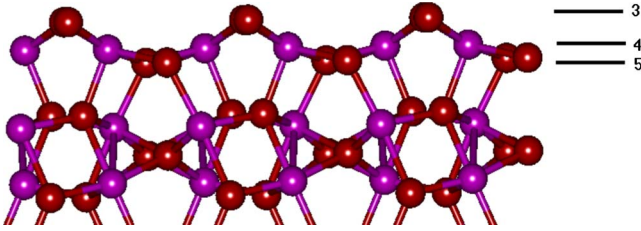


FIG. 5. (Color online) Same as Fig. 2 for $B1$: $X-X-O_2-Al_2-O_2-R$.

B. $\alpha-Al_2O_3$ ($1\bar{1}02$) surface models

We follow the previous experimental^{19–21,34} and theoretical studies^{24,40,41} of the $\alpha-Al_2O_3$ ($1\bar{1}02$) and analogous hematite surface³⁷ to constrain the set of structural models used in the present study.

1. (1×1) surface terminations

We arrive at nine unique (in terms of stoichiometry and/or protonation state) surface terminations of $\alpha-Al_2O_3$ ($1\bar{1}02$) that are possible candidates for the clean and hydrated terminations. Using the same stoichiometry and nomenclature as Lo and co-workers,³⁷ surface models containing all of the atomic layers found in the stoichiometric termination are labeled as A (Figs. 2–4). The clean stoichiometric termination, labeled as model $A1$, is shown in Fig. 2, along with the atomic layer numbering scheme used to define the surface terminations. The surface model terminated at layer-3 O, thus missing the two topmost atomic layers, is labeled as $B1$ (Fig. 5). The $B1$ stoichiometry, $X-X-O_2-Al_2-O_2-R$, can be

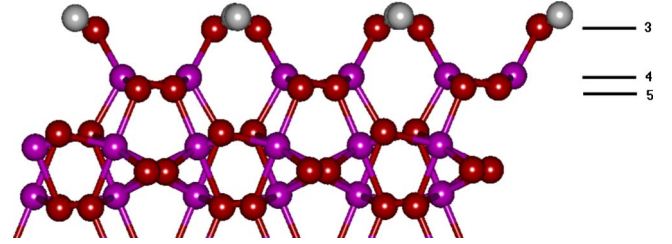


FIG. 6. (Color online) Same as Fig. 2 for $B2$: $X-X-(OH)_2-Al_2-O_2-R$.

made charge-neutral by the addition of two hydrogens, as in the $B2$ model (Fig. 6). The surface models with zero occupancy of the layer-2 Al ions, but retaining the layer-1 O ions, are collectively labeled as C . (The B and C series are also referred to as “missing-Al” or “half-step” terminations.) All of the models are listed in Table I. In each, the overall slabs of substrate plus any water dissociation products are set to be charge neutral. In our notation for the surface stoichiometry, boldface is used to denote the addition of dissociation products, and the repeating bulk sequence ($O_2-Al_2-O_2-Al_2-O_2$) is abbreviated as R . Detailed discussion of the origins and rationalizations of the ($1\bar{1}02$) surface models can be found in the previous study of Lo and co-workers,³⁷ and is repeated here for the nine models considered for $\alpha-Al_2O_3$ ($1\bar{1}02$).

As discussed by Lo *et al.*, some of the surface models posed for the hematite surface impose higher oxidation states on surface Fe cations. In the case of alumina, it is highly unlikely that the Al cation will be further oxidized. The bonding in alumina relative to hematite is highly ionic as the Al d orbitals are too high in energy to afford significant over-

TABLE I. Surface models for the clean and hydrated $\alpha-Al_2O_3$ ($1\bar{1}02$). The atoms in boldface denote layers added above the top layer of the stoichiometric termination and X is used to indicate zero occupancy for an atomic layer that would be present in bulk layering. The repeating bulk sequence ($O_2-Al_2-O_2-Al_2-O_2$) is abbreviated as R .

Model	Layer sequencing for modeled terminations						R
	i	1	2	3	4	5	
$A1$		O_2	Al_2	O_2	Al_2	O_2	R
$A2$	O_2	O_2	Al_2	O_2	Al_2	O_2	R
$A3$	$(HO)_2$	O_2	Al_2	O_2	Al_2	O_2	R
$B1$		X	X	O_2	Al_2	O_2	R
$B2$		X	X	$(OH)_2$	Al_2	O_2	R
$C1$		O_2	X	O_2	Al_2	O_2	R
$C2$		$(HO)_2$	X	$(HO)_2$	Al_2	O_2	R
$C3$		$(HO)_2$	X	$(HO)_2$	Al_2	$(HO)_2$	R
$C4$		$(H_2O)_2$	X	$(HO)_2$	Al_2	O_2	R
Vacancy models							
$A1V1$		O_3	Al_4	O_4	Al_4	O_4	R
$A1V2$		O_2	Al_4	O_4	Al_4	O_4	R
$B1V1$		X	X	O_3	Al_4	O_4	R
$B1V2$		X	X	O_2	Al_4	O_4	R

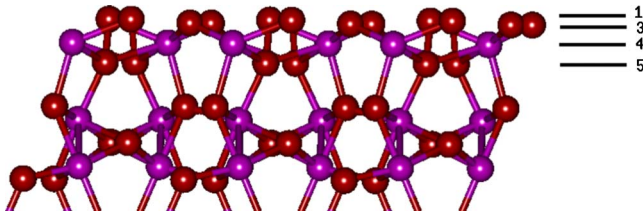


FIG. 7. (Color online) Same as Fig. 2 for C1: $O_2\text{-X-O}_2\text{-Al}_2\text{-O}_2\text{-R}$.

lap with oxygen orbitals. As such, we expect that these surface models (labeled as A2, B1, C1, and C2, with stoichiometries listed in Table I and details given below) will exhibit structural and thermodynamic trends different from what is reported on the analogous hematite surface. These surface models are included for completeness as well as to assess their structure (which is expected to vary notably from the analogous hematite given the inability of Al to further oxidize with added O).

In the stoichiometric A series, adsorption of atomic O at the Al lattice sites in A1 yields model A2: ($O_2\text{-O}_2\text{-Al}_2\text{-O}_2\text{-Al}_2\text{-O}_2\text{-R}$). Heterolytic water dissociation at each of the terminal A1 Al-sites yields model A3: [$(HO)_2\text{-(HO)}_2\text{-Al}_2\text{-O}_2\text{-Al}_2\text{-O}_2\text{-R}$], where boldface is used to denote layers added above the top layer of the stoichiometric termination.

In the C series, the vacancy of the layer-2 Al is modeled. This stoichiometry can equivalently be considered as removal of this layer from the A series or as the addition of dissociated oxygen or H_2O at the fivefold-coordinated Al sites of the B1 model. Capping the layer-1 and layer-3 oxygen atoms in C1 (Fig. 7) with H^+ results in the C2 model: $(HO)_2\text{-X-(HO)}_2\text{-Al}_2\text{-O}_2\text{-R}$, Fig. 8. C2 can be interpreted as heterolytic water dissociation at each of the fivefold-coordinated Al cations of B1. A more likely scenario is the addition of three H^+ for each Al^{3+} vacancy, thus allowing all remaining Al cations to exist in the (III) oxidation state. Both C3 (Fig. 9) and C4 (Fig. 10) achieve this balance but in different ways: in model C3, the layer-1, -3, and -5 oxygen atoms form hydroxyl groups, resulting in $(HO)_2\text{-X-(HO)}_2\text{-Al}_2\text{-(HO)}_2\text{-R}$. In model C4, the layer-5 oxygen atoms remain unprotonated while the layer-1 oxygen atoms form aquo groups, thus allowing coordination between terminating Al and a water layer, written as $(H_2O)_2\text{-X-(HO)}_2\text{-Al}_2\text{-O}_2\text{-R}$.

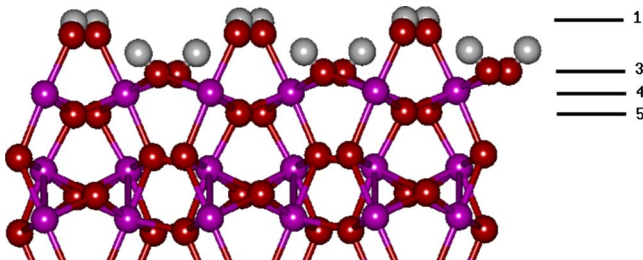


FIG. 8. (Color online) Same as Fig. 2 for C2: $(HO)_2\text{-X-(HO)}_2\text{-Al}_2\text{-O}_2\text{-R}$.

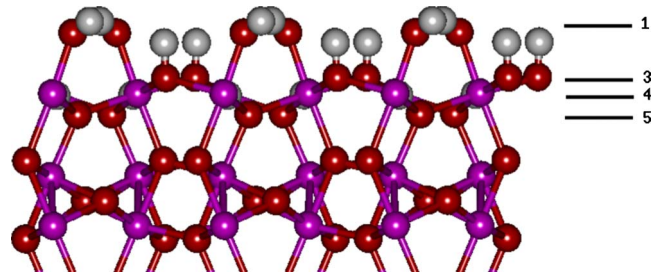


FIG. 9. (Color online) Same as Fig. 2 for C3: $(HO)_2\text{-X-(HO)}_2\text{-Al}_2\text{-(HO)}_2\text{-R}$.

2. (2×1) defect surfaces

At an annealing temperature of 2000 K, Gillet *et al.* report a (2×1) reconstruction of the $\alpha\text{-Al}_2\text{O}_3$ ($1\bar{1}02$) surface.²¹ To investigate the (2×1) reconstruction, we create models for defective surfaces by constraining our efforts to ordered oxygen vacancies in (2×1) cells. As water dissociation products will not persist under the high-temperature annealing conditions that result in the reconstruction, we form oxygen-deficient models starting from both the clean stoichiometric model A1 and the missing-Al model in which the outermost oxygen layer has also been lost, B1. To arrive at (2×1) defect patterns, we either remove a single O from the (2×1) cell, as in the A1V1 and B1V1 models [Figs. 11 and 12], or by removing one O from each (1×1) subcell from alternating O sites as in the A1V2 and B1V2 models [Figs. 11 and 12]. All four defect models start from a (1×1) surface and, through either single or double-oxygen vacancies, form (2×1) surfaces. Included in our investigation is the (2×1) structure, here termed A1V1, proposed by Gillet and co-workers to explain the RHEED pattern.²¹ The additional three defect models are of our design and include a charge-neutral (B1V2) model. By modeling a total of four defect surfaces, we can better assess the stability of oxygen-vacancy structures relative to the clean stoichiometric surface.

III. RESULTS AND DISCUSSION

Side views of the terminating layers of the surfaces listed in Table I are shown in Figs. 2–10. The surface-layer spacings in the optimized geometries are presented in Tables II–IV for the A, B, and C models, respectively. Structural details and 0 K surface-free energies are discussed first, fol-

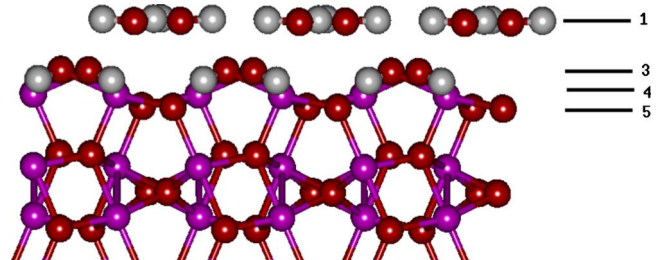


FIG. 10. (Color online) Same as Fig. 2 for C4: $(H_2O)_2\text{-X-(HO)}_2\text{-Al}_2\text{-O}_2\text{-R}$.

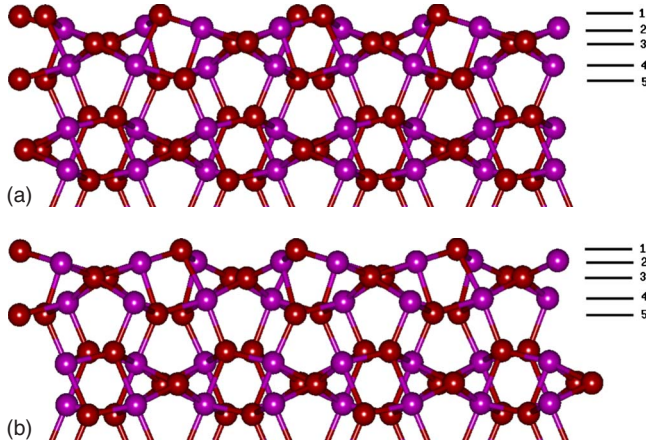


FIG. 11. (Color online) Single-oxygen-vacancy models, showing two repeats of the (2×1) cell. (a) Single-vacancy model A1V1 ($O_3-Al_4-O_4-Al_4-O_4-R$) (b) Double-vacancy model A1V2 ($O_2-Al_4-O_4-Al_4-O_4-R$).

lowed by the results of *ab initio* thermodynamic analysis to investigate the stability under different conditions.

A. Structural optimizations

We characterize the DFT-optimized geometries for all of the modeled $\alpha-Al_2O_3$ ($1\bar{1}02$) surfaces by calculating the relaxed spacings between atomic layers and the percent deviation from the theoretical bulk spacings in Table II for the A models, Table III for the B1 model, Table IV for the C models, and Table V for the defect surface models. Notable cases that show significant in-plane relaxations are also discussed.

1. (1×1) surface terminations

The clean stoichiometric surface model (A1) exhibits an outward relaxation of 17% relative to the bulk in the terminal layer 1-2 O_2-Al_2 , and a compression of 29% relative to the bulk in the subsequent layer 2-3 Al_2-O_2 . The terminal surface atoms have a reduced coordination relative to the bulk and thus a contractive relaxation is predicted for the outermost layers. This is well documented in the Al-terminated $\alpha-Al_2O_3$ (0001) surface under UHV conditions, in which the

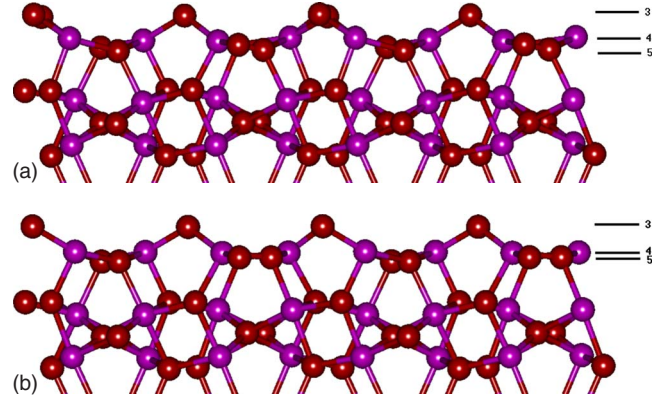


FIG. 12. (Color online) Double-oxygen-vacancy models, showing two repeats of the (2×1) cell. (a) Single-vacancy model B1V1 ($X-X-O_3-Al_4-O_4-R$) (b) Double-vacancy model B1V2 ($X-X-O_3-Al_4-O_4-R$).

outermost layer relaxes to about -85% of its bulk value.^{23,58} The higher index ($1\bar{1}02$) face is open enough to allow for greater in-plane relaxations. Here, the counter-intuitive surface expansion is explained by the lateral-surface relaxations. We measure a 3.3% and $\pm 5.6\%$ in-plane relaxation in the layer-1 O positions and layer-2 Al positions, respectively. This is similar to the theoretical results of Lo *et al.*, which reported +37% and -26% relaxations between the terminal O_2-Fe_2 and Fe_2-O_2 layers, accompanied by 3.0% and $\pm 5.0\%$ in-plane relaxation in the layer-1 O positions and layer-2 Fe positions, respectively, on the isostructural $\alpha-Fe_2O_3$ ($1\bar{1}02$) surface. As in the hematite surface, these in-plane distortions result in surface Al-O distances that are shorter than in the bulk, stabilizing the reduced surface oxygen coordination.

When atomic O is modeled at the Al lattice sites in A1 to form A2, the resulting optimized structures are distinct between the two corundum oxides, as predicted based on the inability of Al^{3+} to further oxidize. As reported by Lo *et al.*, the hematite A2 model exhibits short terminal Fe-O groups, not dissimilar to the ferryl ($Fe=O$) groups on the $\alpha-Fe_2O_3$ (0001) surface.^{57,59} While such $M=O$ terminations at certain oxygen pressures are thought to be stable for transition-metal corundum oxides,⁶⁰ the Al *s* and *p* orbitals are utilized. The Al *d* orbitals are too high to overlap with oxygen *p* orbitals

TABLE II. Calculated layer spacings (\AA) and percent relaxations with respect to theoretical bulk spacing ($\% \Delta$) for stoichiometric (A) models. Surface stoichiometries are discussed in the text and listed in Table I. Experimental values are for the stoichiometric model in Ref. 19.

Layers		A1	$\% \Delta$	A2	$\% \Delta$	A3	$\% \Delta$	Expt.	$\% \Delta$
<i>i</i> -1				0.926		1.296			
1-2	O_2-Al_2	0.417	+17	0.264	-26	0.288	-19	0.031	-91
2-3	Al_2-O_2	0.510	-29	0.988	+37	0.818	+13	1.169	+64
3-4	O_2-Al_2	0.778	+8	0.710	-2	0.734	+2	0.424	-40
4-5	Al_2-O_2	0.458	+29	0.284	-20	0.313	-12	0.324	-9
5-6	O_2-O_2	1.285	-6	1.403	2	1.394	+1	1.365	+1
6-7	O_2-Al_2	0.398	+12	0.337	-5	0.340	-5	0.333	-6
7-8	Al_2-O_2	0.723	0	0.721	0	0.721	0	0.814	+14

TABLE III. Calculated layer spacings (\AA) and percent relaxations with respect to theoretical bulk spacing ($\% \Delta$) for the B1 model. Surface stoichiometries are discussed in the text and listed in Table I.

Layers		B1	$\% \Delta$	B2	$\% \Delta$
3-4	O ₂ -Al ₂	0.732	+2	1.425	+98
4-5	Al ₂ -O ₂	0.365	+2	0.328	-8
5-6	O ₂ -Al ₂	1.377	0	1.303	-5
6-7	Al ₂ -O ₂	0.318	-11	0.392	+10
7-8	O ₂ -O ₂	0.751	4	0.733	2

to stabilize the Al=O structure. Instead, we observe in the alumina A2 model that the added atomic oxygen is displaced away from the Al cation to the triply-coordinated surface oxygen on the neighboring Al site (Fig. 3), resulting in an O-O distance of only 1.54 \AA . This short O-O distance is only about 30% greater than the molecular O₂ double bond, indicating that the modeled atomic O adsorption is only slightly stable relative to a free O₂ molecule. Thus the A1 surface may not be quite able to fully dissociate O₂. On the hematite A2 model, the shortest distance between singly- and triply-coordinated oxygen atoms is 2.83 \AA , and occurs between singly- and triply-coordinated oxygen atoms on the same Fe cation. The analogous O-O distance between neighboring singly- and triply-coordinated oxygen atoms on the A2 hematite model is 3.24 \AA . This result has implications for the surface reactivity of alumina. Surface Al(III) is a very poor electron donor and O is not a strong enough oxidant to force strong electron sharing or donation between species.

In the A3 model, the addition of protons stabilizes the otherwise unsaturated layer-*i* O atoms and the optimized structure is again highly analogous to the corresponding hematite surface. The layer 1-2 (O₂-Al₂) relaxation is -19%, and the layer 2-3 (Al₂-O₂) relaxation is +13%, nearly identical to the respective hematite values of -19% and +12% reported by Lo *et al.*). Likewise, the terminal Al-O distances are 1.81 \AA , similar to the appropriate bulk comparison values observed for the terminal Fe-O distances.

The difficulty of oxidizing Al³⁺ also results in the B1, C1, and C2 models adopting an unstable oxygen coordination. On the B1 surface, we do not observe large surface relaxations between the outer layers (Table III). However, significant in-plane distortions occur such that the terminal oxygen atoms form a near-perfect row along the $[\bar{1}101]$ direction. In the resulting structure, the oxygen atoms along this row form

similar bonds with neighboring Al cations of 1.85 and 1.87 \AA . The analogous hematite B1 model exhibits a -23% layer 3-4 O₂-Fe₂ relaxation and the terminal Fe-O distances are 1.72 and 2.10 \AA . The small outer layer expansion on alumina, along with the unique near-row arrangement of layer-3 O on alumina, demonstrate a structural compromise to accommodate the excess oxygen. On the C1 surface, we again observe short O-O distances (1.45 \AA or 20% expansion of the molecular O₂ double-bond distance). In other words, we again observe that adsorbed O finds structural O a better electron donor than Al. As observed on the A2 surface, the singly-coordinated terminal oxygen atoms displace both in- and out-of-plane away from the cations. On C1, the migration is to the layer-3 doubly-coordinated oxygen layer. The analogous O-O distance on C1 hematite is 2.54 \AA , more than 1 \AA greater than on alumina.

In the B2 model, the excess oxygen in the B1 stoichiometry is compensated by hydrogen, and the resulting surface model is charge-neutral, with tetrahedral surface Al. The addition of hydrogen to the B1 stoichiometry has a notable effect on the surface relaxations in B2. As can be seen in Table III, the B2 model exhibits greater relaxation between the atomic layers than in the oxygen-rich B1 model. However, as the layer-3 oxygen atoms in B2 exist as hydroxyl groups, the in-plane relaxations are distinct between the two models, with the terminal oxygen atoms remaining singly coordinated to Al cations with optimized short (between Al and coordinating oxygen) and long (between Al and neighboring oxygen) layer 3-4 O-Al distances of 1.72 and 3.23 \AA . The 1.81 \AA Al-OH bond distance on the A3 surface is notably longer than the 1.72 \AA B2 Al-OH bond distance, consistent with the decrease in the coordination of the surface Al cations from sixfold in A3 to fourfold in B2.

Comparison of surface relaxations in the C2, C3, and C4 surface models (Table IV) shows how the extent and type of

TABLE IV. Calculated layer spacings (\AA) and percent relaxations with respect to theoretical bulk spacing ($\% \Delta$) for missing-Al (C) models. Surface stoichiometries are discussed in the text and listed in Table I. Experimental values are for the missing-Al model in Ref. 19.

Layers		C1	$\% \Delta$	C2	$\% \Delta$	C3	$\% \Delta$	C4	$\% \Delta$	Expt.	$\% \Delta$
1-3	O ₂ -O ₂	0.102	-93	1.144	-17	1.256	-9	1.425	+4	1.460	+6
3-4	O ₂ -Al ₂	0.595	-17	0.557	-23	0.436	-40	0.440	-39	0.368	-48
4-5	Al ₂ -O ₂	0.584	+64	0.589	+66	0.593	+67	0.340	-4	0.465	+31
5-6	O ₂ -O ₂	1.315	-4	1.239	-10	1.283	-7	1.378	0	1.200	-11
6-7	O ₂ -Al ₂	0.389	+8	0.361	+2	0.436	+23	0.356	0	0.403	+14
7-8	Al ₂ -O ₂	0.679	-6	0.743	+3	0.686	-5	0.729	+1	0.781	+10

TABLE V. Calculated layer spacings (\AA) and percent relaxations with respect to theoretical bulk spacing ($\% \Delta$) for the vacancy models. Surface stoichiometries are discussed in the text and listed in Table I.

Layers		A1V1	$\% \Delta$	A1V2	$\% \Delta$	B1V1	$\% \Delta$	B1V2	$\% \Delta$
1-2	O ₂ -Al ₂	0.408	+12	0.412	+13				
2-3	Al ₂ -O ₂	0.525	-27	0.532	-26				
3-4	O ₂ -Al ₂	0.791	+10	0.802	+11	0.789	+9	0.845	+17
4-5	Al ₂ -O ₂	0.450	+23	0.447	+23	0.299	-16	0.239	-33
5-6	O ₂ -O ₂	1.295	-6	1.299	-5	1.389	+1	1.405	+2
6-7	O ₂ -Al ₂	0.392	+7	0.390	+7	0.327	-8	0.331	-7
7-8	Al ₂ -O ₂	0.725	+1	0.725	+1	0.755	+5	0.739	+2

surface oxygen functional group protonation influences the optimized atomic layer spacings. While C2 and C3 have a different number of surface protons (Table I), the reported surface relaxations are qualitatively similar. Both exhibit large layer 3-4 (O₂-Al₂) compression and large layer 4-5 (Al₂-O₂) expansions, -23% and +66%, respectively on C2, and -40% and +67%, respectively on C3. In both surface models, the Al-vacancy in layer 2 is compensated by simultaneous layer-3 oxygen relaxation into the bulk, and layer-5 Al expansion toward the vacancy layer. These results are strongly comparable to the commensurate hematite relaxations for both C2 and C3.

The fact that C2 and C3 are similar in surface relaxation patterns despite the varying protonation states between the two models is suggestive of interesting surface reactivity. We interpret the anomalous structural agreement between C2 and C3 to imply that the hydroxy radical is semistable as an adsorbed species. This may help explain some of the catalytic activity of alumina with respect to electron-transfer reactions⁶¹ despite the fact that Al is not redox labile.

The C4 relaxation pattern is distinct from the other C models. As can be seen in Table IV, the layer 3-4 (O₂-Al₂) compression is similar across the C series. The C4 disparity appears in the layer 4-5 Al₂-O₂ relaxation, which is -4% in C4. This value is at least 93% smaller in magnitude and of opposite sign compared to the other models in the C series. As can be seen in Fig. 10, the protons on the double-coordinated layer-3 oxygen atoms are directed into the surface layer-5 triply-coordinated O layer, indicative of intrasurface hydrogen bonding in this surface model. The layer-3 OH bond distance is 1.01 \AA and the distance between the protons and the layer-5 O is 1.64 \AA . The influence of surface hydroxyl group orientation on surface stability has been observed and discussed on similar hydrated surfaces.^{62,63} A final consideration of the C4 structure is the Al-O distance between the layer-4 Al and the aquo groups. The distance in the optimized structure is 2.22 \AA , longer than bulk-like Al-O distances. This raises the question as to how strongly the terminal water layer is bound. To address this, we carried out a series of tests in which we moved the water layer in 0.1 \AA increments in the direction of the surface normal. We then computed single-point energy calculations (that is, with no structural optimization) and compared the DFT energies. When we move the H₂O layer by -0.1, 0.0, 0.1, and 0.2 \AA along the surface normal relative to the optimized C4 struc-

ture, the resulting changes in energy were 0.07, 0.00, 0.17, and 0.19 eV, respectively. This Morse-type potential energy profile supports that the H₂O layer is coordinated with the surface as the total energy would be unaffected by outward displacements of an uncoordinated H₂O layer. On the hematite analog, the terminal Fe-O bond length of 2.42 \AA is also uncharacteristically long compared to bulklike values. However, we computed a similar Morse-type potential energy profile, again varying the height of the H₂O layer with respect to the hematite surface. Therefore, the C4 models have aquo groups coordinating with the outermost cation layer and are distinct from a surface model plus a water layer interacting only through water-surface hydrogen bonding or electrostatic interactions. From the above structural analysis and considerations of Al and O coordination in the various surface models, we can expect that some of the strongly oxidized surfaces (such as A1, B1, and C1) will be less stable than modeled protonations of these base stoichiometries (such as A3, C3, and C4). In the following sections, we present and discuss the results of our *ab initio* thermodynamics analysis on these surface models, first at 0 K and then under both UHV and environmentally relevant conditions.

2. (2 \times 1) defect surfaces

Details of the relaxed spacings between atomic layers and the percent deviation from the theoretical bulk spacings for the defect surfaces are presented in Table V. No experimental structural data is available for comparison for these defect surfaces. The defective surfaces also exhibit local relaxations in the defect vicinity and the optimized terminal Al-O distances near the oxygen vacancies show trends based on the defect stoichiometries. In the A1V1 and A1V2 models, oxygen is being removed from the initially charge-neutral A1 model, leading to undercoordinated layer-2 Al cations. To compensate for the underbonded Al cations, the remaining layer-1 oxygen atoms in the vacancy subcell(s) form longer bonds with nearest-neighbor layer-2 cations (up to 1.91 \AA in both A1V1 and A1V2 relative to 1.797 \AA and 1.861 \AA in A1) and shorter bonds with second-neighbor layer-2 cations (4.51 \AA and 4.46 \AA in A1V1 and A1V2, respectively, compared with 4.57 \AA in A1). In the B1V1 and B1V2 models, oxygen is being removed from the excess-oxygen stoichiometry of the B1 model, with the double-vacancy model B1V2 being charge-neutral. As such, an opposite trend is observed relative to the A series vacancy models. The nearest-neighbor

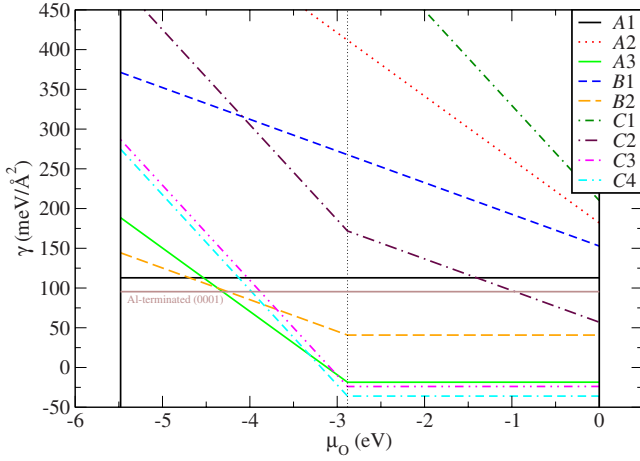


FIG. 13. (Color online) Free energies of various surface termination models for α - Al_2O_3 ($1\bar{1}02$), and the Al-terminated (0001) surface, as determined by *ab initio* thermodynamics. Surface stoichiometries are discussed in the text and listed in Table I.

layer 3-4 Al-O distances decrease in the vacancy subcell(s) from 1.85 and 1.87 Å in B1, to 1.81 and 1.83 Å in B1V1, to 1.76 and 1.77 Å in B1V2. Consistently, the shortest second-neighbor layer 3-4 Al-O distances increase from 4.1 Å in B1, to 4.32 Å and 4.42 Å in B1V1 and B1V2, respectively. The changes in terminal Al-O bond distances and Al coordination foreshadow the role of ΔG^{vib} in the thermodynamic stability of the defect surfaces as a function of temperature.

B. Surface-free energies at 0 K

Whereas relaxations constitute the most direct link of theory with experiment, the *ab initio* thermodynamic analysis of the surface-free energies provide the insight as to the underlying physics that makes one surface more stable than another under given environmental or preparation conditions. Calculated values of surface-free energies γ using Eq. (10) at 0 K at the oxygen-poor and oxygen-rich limits are plotted in Fig. 13. Included are the nine α - Al_2O_3 ($1\bar{1}02$) models listed in Table I as well as the clean Al-terminated α - Al_2O_3 (0001) surface for comparison.⁶⁴

Over the full range of accessible μ_{O} , the surfaces that minimize the surface-free energy are stoichiometric [A1, and Al-terminated (0001)] or sufficiently protonated to saturate surface oxygen (A3, C3, and C4). This is consistent with results reported in Refs. 40 and 41, which carried out similar analyses but with only one and two hydroxylated surface models, respectively. Our results show that the ratio of the A1 surface energy relative to the (0001) surface is 1.18, in good agreement with the theoretical values of 1.03 and 1.02 (Marmier and Parker,⁴⁰ and Briquet *et al.*,⁴¹ respectively) and the experimental value of 1.05.⁶⁵ In terms of absolute theoretical values, our results (and those of Marmier and Parker followed by those of Briquet *et al.* in parenthesis) of 112.8 (127.3, 106.7) $\text{meV}/\text{\AA}^2$ for the ($1\bar{1}02$) surface, and 95.4 (123.6, 104.2) $\text{meV}/\text{\AA}^2$ for the and (0001) surface, also agree well.

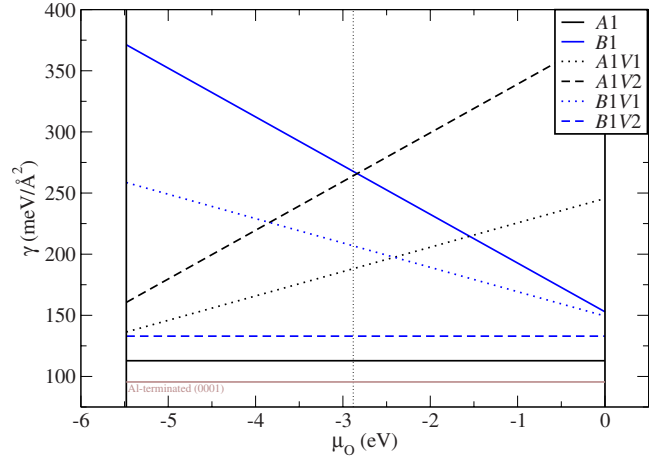


FIG. 14. (Color online) Free energies of clean and oxygen-vacancy surface termination models for α - Al_2O_3 ($1\bar{1}02$) as determined by *ab initio* thermodynamics at 0 K. Surface stoichiometries are discussed in the text and listed in Table I.

Relative to the stoichiometric references, and in the oxygen-poor range of Fig. 13, the surface models with excessive oxygen (A2, A3, B1, C1, C2, C3, and C4) all show a negative slope with respect to increasing μ_{O} , as is intuitive for these already oxidized surfaces. In the oxygen-rich regime, in equilibrium with H_2O , the values of $\gamma(0 \text{ K})$ for A3, B2, C3, and C4 become constant, as governed by stoichiometry and Eq. (10).

In Fig. 14, we present the results for $\gamma(0 \text{ K})$ of the clean stoichiometric surface, A1, the clean missing-Al model B1, and the four defect models derived from these stoichiometries (single-vacancy models A1V1 and B1V1, and double-vacancy models A1V2 and B1V2). The Al-terminated (0001) surface value for $\gamma(0 \text{ K})$ is again included for comparison as it is a commonly observed alumina termination. This set of surface stoichiometries span charge-neutral models (A1, B1V2, Al-terminated (0001)), oxygen-deficient models (A1V1, A1V2), and oxygen-rich models (B1, B1V1). As such, we see zero, positive, and negative slopes in $\gamma(0 \text{ K})$ as a function of μ_{O} , respectively. While none of the four defect surfaces compete with the clean stoichiometric A1 surface, $\gamma(0 \text{ K})$ of the charge-neutral B1V2 model is only 20.1 $\text{meV}/\text{\AA}^2$ higher than that of the A1 model. This is similar to the 17.41 $\text{meV}/\text{\AA}^2$ difference in $\gamma(0 \text{ K})$ between the A1 model and the lower-energy Al-terminated (0001) surface.

C. Thermodynamic stability at finite T

We aim to determine how the thermodynamic stability of the structural models varies with temperature under both UHV and ambient conditions. In doing so, we can suggest whether thermodynamic or kinetic factors, i.e., surface preparations and/or measurement conditions, exert control on the preferred structural phase.

1. Modeled UHV conditions

We first discuss the relative stability of the (2×1) defect structures relative to the clean stoichiometric A1 model as a

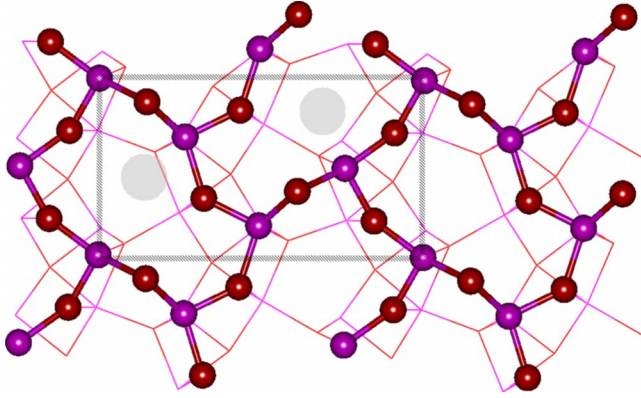


FIG. 15. (Color online) Top view of the optimized $B1V2$ double-oxygen-vacancy model. The first layer-3 O, layer-4 Al, and layer-5 O are shown in a ball-and-stick representation while layer-6 (O), layer-7 (Al), layer-8 (O), and layer-9 (Al) atoms are shown in a line representation. The (2×1) cell is indicated by the dashed rectangle. The large gray circles within the unit cell indicate the vacancy sites.

function of temperature. Only the charge-neutral $B1V2$ model (the top view showing vacancy locations is shown in Fig. 15) is thermodynamically competitive with the $A1$ model so we limit our discussion to these two surfaces. The results for $\gamma(T)$ for $A1$ and $B1V2$ are presented in Fig. 16. Note that as dictated by the model stoichiometries, there is no dependence on the pressure of any gas-phase species. The temperature dependence is instead governed by enthalpic and entropic changes in $\mu_{\text{Al}_2\text{O}_3}$ and ΔG^{vib} (Eq. (3)) as a function of T . The former causes an increase in $\gamma(T)$ while the later reduces the value of $\gamma(T)$. As shown in Fig. 16, the competitive effects of temperature on the relative stabilities of the $A1$ and $B1V2$ models leads to a crossover at 2763 K. We note that without inclusion of the ΔG^{vib} term, the model would not predict this crossover. While the ΔG^{vib} term is known to be of great importance in predicting the stability of hydroxy-

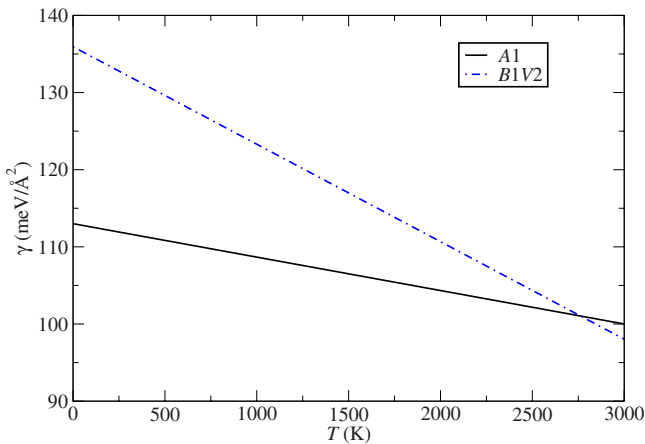


FIG. 16. (Color online) Free energies of the clean stoichiometric termination ($A1$) and the charge-neutral (2×1) ordered oxygen-vacancy defective $\alpha\text{-Al}_2\text{O}_3$ ($1\bar{1}02$) model ($B1V2$) as determined by *ab initio* thermodynamics as a function of temperature T . Surface stoichiometries are discussed in the text and listed in Table I.

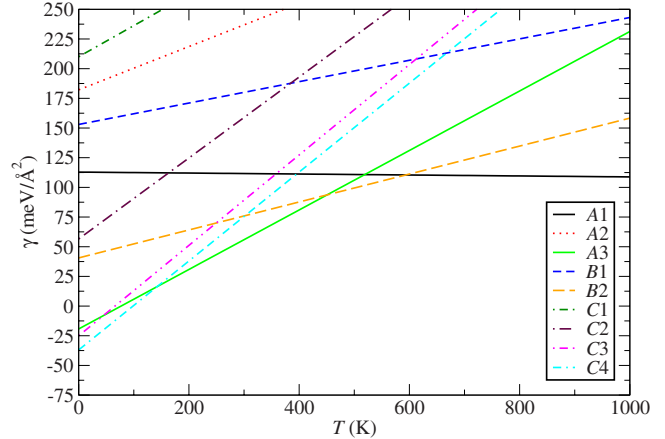


FIG. 17. (Color online) Free energies of various surface termination models for $\alpha\text{-Al}_2\text{O}_3$ ($1\bar{1}02$) as determined by *ab initio* thermodynamics, $p_{\text{O}_2}=p_{\text{H}_2\text{O}}=10^{-8}$ kPa at all temperatures. Surface stoichiometries are discussed in the text and listed in Table I.

lated surfaces,⁵³ this case highlights the importance of the entropy in a hydrogen-free but open, defective surface. Our prediction that the (2×1) defective surface becomes more stable than the clean stoichiometric (1×1) surface is in qualitative agreement with the RHEED study that reports a (2×1) pattern when samples are annealed at 2000 K but not when the annealing temperature is 1100 K.²¹ Quantitatively, our predicted crossover temperature is higher than the experimental annealing temperature. Given the omission of both kinetic effects and melting of Al and Al_2O_3 solid phases, the accuracy of the employed model is expected to worsen with increasing T . We therefore consider the qualitative prediction that the charge-neutral $B1V2$ double-vacancy (2×1) model become more stable relative to the stoichiometric $A1$ model at high temperature to be within reasonable agreement with the experimental observation of a (2×1) surface after annealing at 2000 K.

We next consider the (1×1) surfaces and select various conditions to recreate the ranges encountered in typical experiments. The first set of conditions we model are UHV O_2 and H_2O pressures ($p_{\text{O}_2}=p_{\text{H}_2\text{O}}=10^{-10}$ bar) and varying T up to 1000 K (and thus below the melting temperature of $\alpha\text{-Al}_2\text{O}_3$). These conditions are meant to bracket the preparation and measurement conditions likely used in UHV surface preparation and measurements. The calculated values of γ as a function of T are presented in Fig. 17. We predict four different terminations to be the stable within different temperature ranges. From 0 to 142 K, the $C4$ model has the minimum value of γ . From 142 to 451 K, the $A3$ model is preferred. Between 451 and 593 K, the $B2$ surface is the predicted thermodynamically stable model. Finally, at $T > 593$ K, the clean stoichiometric model $A1$ is predicted to be the most stable.

In addition to the minimum energy crossings, we also predict that five surfaces cross the energy of the $A1$ model at different temperatures: $B2/A1$ at 593 K, $A3/A1$ at 519 K, $C4/A1$ at 396 K, $C3/A1$ at 358 K, and $C2/A1$ at 163 K. This suggests that thermodynamically driven phases transitions between a hydrated “missing-Al” model and hydrated stoi-

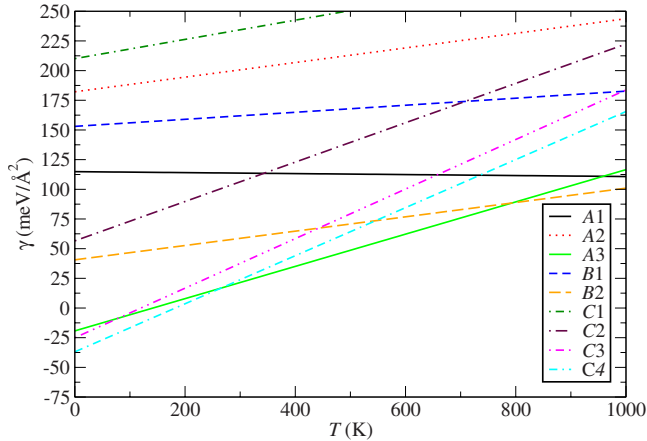


FIG. 18. (Color online) Free energies of various surface termination models for α - Al_2O_3 ($1\bar{1}02$) as determined by *ab initio* thermodynamics, $p_{\text{O}_2}=20$ kPa and $p_{\text{H}_2\text{O}}=3.2$ kPa at all temperatures. Surface stoichiometries are discussed in the text and listed in Table I.

chiometric model could occur in two ways: directly at the A3/C4 crossover temperature of 142 K, or by first heating A3 to above 593 K. The later path would first drive off the water dissociation products and result in the A1 structure, which when cooled comes into equilibrium with B2, A3, C4, C3, and C2. Kinetic barriers are not accounted for, hence surface preparations that may lead to different stable or metastable configurations under certain conditions could be locked in depending on the range of temperatures used in the preparation.

2. Modeled ambient conditions

Next, we consider conditions consistent with “wet” sample preparation and surface measurements. We set p_{O_2} to an ambient 20 kPa and the corresponding saturated H_2O vapor pressure at 298.15 K is 3.2 kPa. In doing so, we model the surface being heated while the gas environment effectively remains cold. We are not modeling a closed system but instead are approximating experimental conditions; hence we fix both of these pressures and vary the temperature. This is a reasonable recreation of experimental conditions under which *in situ* measurements are made. The resulting values of γ as a function of temperature are shown in Fig. 18. We focus on the difference between the most preferred C-series model (C4) and the most preferred A-series model (A3). At room temperature (298.15 K), the C4 model is preferred by just 1.8 $\text{meV}/\text{\AA}^2$ relative to the A3 model. At $T=265$ K, there is a crossover and the A3 model becomes the minimum energy structural model. This crossover occurs well below the temperatures used in the experiments of Catalano and co-workers, and no additional crossovers occur until much higher temperature (for example, A3 intersects B2 at 793 K, which intersects A1 at 1152 K). Therefore our *ab initio* thermodynamic predictions under ambient air conditions are consistent with the results of Catalano *et al.*, showing that a stoichiometric termination with an additional oxygen layer is preferred. Consistent with the study by Marmier and Parker⁴⁰

[in which two Al_2O_3 ($1\bar{1}02$) surfaces corresponding to our A1 and A3 models were studied], and that of Briquet and co-workers⁴¹ [in which three Al_2O_3 ($1\bar{1}02$) surfaces corresponding to our A1 and A3 models and a third partially hydroxylated model were studied] we predict that this A3 termination is fully hydroxylated. In fact, the crossover temperature between our A3 and A1 models at 958 K is in truly excellent agreement with the calculated crossover temperature of 969 K between analogous models by Briquet and co-workers.⁴¹ Our comprehensive study with a total of nine (1×1) surface models and four defective (2×1) surfaces provides additional information about the surface stability. The crossover between A3 and C4 reported here is qualitatively similar to predictions made on the analogous hematite surface. Lo *et al.* report that under the same conditions, the C4 surface is the most stable up to 435 K, at which point the A3 termination becomes the most lowest energy configuration.

Our model predictions show that the hydroxylated surfaces A3, B2, C3, and C4 are the most stable at room temperature, consistent with the results of other similar studies on hydrated metal-oxide surfaces.^{30,37,40,47} The calculated values of γ show that at 298 K and under UHV, A3 is the most stable, with C4, B2, and C3 18.9, 21.4, and 32.1 $\text{meV}/\text{\AA}^2$ higher, respectively. At 298 K and ambient pressures ($p_{\text{O}_2}=20$ kPa and $p_{\text{H}_2\text{O}}=3.2$ kPa), C4 is the minimum energy structure, with A3 and C3 1.8 and 13.2 $\text{meV}/\text{\AA}^2$ higher, respectively. These competitive minimum energies and the discussed crossovers under both UHV and ambient conditions predict that both surface preparation and measurement conditions influence the thermodynamically preferred structure for hydrated α - Al_2O_3 ($1\bar{1}02$). However, we note that our results do not consider kinetic barriers. In particular, high temperature annealing is likely consistent with significant changes in surface Al and O stoichiometry, which may be kinetically hindered at low temperatures. Hence crossovers between A and C or B series at low temperature may not occur. Instead, relative stabilities should be considered among surfaces that differ by only relatively labile H and O stoichiometry. For example, while the B2 model (with tetrahedral Al surface cations) is not predicted to cross over as the minimum energy structure until at least 593 K under ambient conditions, it should be considered a competitive surface model as it is within approximately 20 $\text{meV}/\text{\AA}^2$ of other surface models at room temperature.

In comparing our results to previous experimental findings, we consider both our DFT surface relaxations (Tables II–IV) and our temperature-dependent surface-free energies (Figs. 17 and 18). Our computed values of γ support observations of both a hydroxylated stoichiometric termination (A3) and hydroxylated missing-Al models (C3 and C4). The A3 surface is the thermodynamically most stable model from $T=142$ to 451 K under UHV or $T>265$ K and up to 793 K under ambient pressures. When the *i*-layer oxygen atoms are not protonated, as in model A2, the surface is thermodynamically unstable. Previous theoretical modeling of the stoichiometric surface is in agreement with the need for the *i*-layer oxygen to be protonated to achieve thermodynamic stability.^{40,41} We also find that the C3 and C4 missing-Al

terminations, similar to the missing-Al model observed by Trainor *et al.* are thermodynamically competitive, and C4 is the minimum energy structure under UHV conditions up to 142 K and ambient conditions up to 451 K.

Interestingly, we find two surface models with identical stoichiometries but distinct proton arrangements (C3, with hydroxyl groups and C4, with hydroxyl and aquo groups) to be within approximately 20 meV/Å² over a range of conditions. In examining the layer spacings for the missing-Al model, our results for C3 (−40%, +67%, −7%, and +23% for layers 3-4, 4-5, 5-6, and 6-7, respectively) are a better match with the corresponding reported fits to crystal truncation rod diffraction data of −48%, +31%, −11%, and +14%. As previously discussed, the modeled C4 surface has a distinct surface relaxation pattern and does not exhibit the large layer 4-5 expansion seen in the C3 model. This coupled with the known dependence of surface structure on preparation³⁸ make both C3 and C4 viable as a reasonable model for hydrated α -Al₂O₃ (1 $\bar{1}$ 02).

IV. CONCLUSIONS

Our *ab initio* thermodynamics analysis of nine Al₂O₃ (1 $\bar{1}$ 02) surface models at 0 K and at two sets of finite T , p conditions indicate that experimental conditions determine surface structure stoichiometry. Over the full range of accessible μ_{O} at 0 K, either bare stoichiometric or hydroxylated surface models are thermodynamically preferred, with a number of thermodynamically predicted crossovers in the minimum energy surface spanning both hydrated stoichiometric and hydrated missing-Al models, at both UHV and ambient conditions. The surface structure can be interpreted as being structurally sensitive to both surface preparation and characterization measurement conditions. Under UHV or ambient conditions up to 600 K, the surface-free energy of the four most stable surface models are all within 75 meV/Å². Of these four models, two are consistent with the missing-Al structure [C3, and C4, with surface stoichiometries of (HO)₂-X-(HO)₂-Al₂-(HO)₂-R, (H₂O)₂-X-(HO)₂-Al₂-O₂-R, respectively], a third is consistent with the A3 surface stoichiometry of (HO)₂-(HO)₂-Al₂-O₂-Al₂-O₂-R, and the last is a charge-neutral stoichiometry with tetrahedral surface Al cations [X-X-(OH)₂-Al₂-O₂-R].

In addition to comparing the thermodynamic stability of clean and hydrated (1 × 1) surfaces, we have also applied the *ab initio* thermodynamic analysis to study defective (2 × 1) α -Al₂O₃ (1 $\bar{1}$ 02) surface with both single- or double-oxygen vacancies. Starting from a missing-Al model, a double-vacancy structure proposed here results in a charge-neutral stoichiometry that we predict becomes more stable than the stoichiometric (1 × 1) surface at high temperature. This is in agreement with the reported observation of a (1 × 1) RHEED pattern after annealing at 1100 K and a (2 × 1) RHEED pattern after annealing at 2000 K,²¹ demonstrating the utility of applying the *ab initio* thermodynamics method to defective surface structures.

Our results indicate that both surface preparation and measurement conditions influence the thermodynamically

preferred surface stoichiometry. This can be seen in the crossovers between the most stable surface structures in our *ab initio* thermodynamics analyses under ambient conditions. Notably, under our modeled *in situ* conditions with p_{O_2} to an ambient 20 kPa and the corresponding saturated H₂O vapor pressure at 298.15 K is 3.2 kPa, we predict that a hydrated missing-Al structure (C4) is preferred from room temperature up to 451 K, at which point a hydrated stoichiometric structure (A3) becomes the minimum energy surface. This result demonstrates that the relative thermodynamic stability of these two surface models can reverse under variations in the measurement conditions.

The fact that several crossovers in surface-free energies occur in our modeled ambient and UHV conditions, including a competitive charge-neutral stoichiometry with fourfold surface Al (model B2) suggests that in addition to measurement conditions, surface preparation conditions will also influence the minimum energy surface stoichiometry. Of course, kinetic limitations, particularly at low temperatures, are likely to result in metastable configurations.

The structural results of our study shed light on key differences between alumina and transition metal-oxide-surface stability. The inability of Al³⁺ to further oxidize with non-protonated oxygen atoms adsorbed in excess of the corundum stoichiometry leads to thermodynamically unstable surfaces. Instead of pairing with surface Al, adsorbed atomic oxygen O_{ads} finds lattice oxygen O_{lattice} to be a better electron donor, resulting in short O_{ads}-O_{lattice} bond distances. On stoichiometric or hydroxylated surfaces, the DFT-optimized structures and layer relaxations relative to bulk are analogous to the hematite analogs.

Surface reactivity predications can be made through analysis of the thermodynamically preferred surface models. The A3 model has both singly- and doubly-coordinated surface hydroxyl groups, while the C3 model has singly-, doubly-, and triply-coordinated hydroxylated groups. Bond-valence predictions of surface functional group reactivity predict that the singly- and triply-coordinated groups to be more reactive relative to doubly-coordinated hydroxyl groups on alumina.³³ On the B2 model, which we predict to be a competitive surface stoichiometry, the terminal oxygen atoms are singly coordinated to tetrahedral Al cations. This surface could exhibit exceptional reactivity compared to the other surface with sixfold Al. Our results that more reactive functional groups are available on the (1 $\bar{1}$ 02) surface, combined with previous results that the most stable (0001) surface under similar conditions has only doubly-coordinated hydroxyl groups^{26,30} could be a partial explanation for the known greater reactivity of the (1 $\bar{1}$ 02) surface toward Pb(II) than on the (0001) surface.²⁵

The variety of protonation states found in the surface oxygen functional groups also has implications for reactivity. The C4 model exhibits several unique traits relative to A3 and C3, including surface-bound aquo groups and intrasurface hydrogen bonding. Using bond valence considerations and the empirical model of Hiemstra *et al.*⁶⁶ to predict pK_a values, the aquo groups are predicted to have a highly labile proton. Studies of Pb(II) on (0001) alumina demonstrate a strong role of surface hydroxyl group orientation on

reactivity.⁶³ The presence of both intrasurface hydrogen bonding and aquo groups could lead to interesting and distinct reactivity on this surface model.

ACKNOWLEDGMENTS

This work was supported by NSF under Grants No.

CBWT-0404400 and No. CHE-0431425, and utilized the high-performance computational capabilities of the Arctic Region Supercomputing Center at the University of Alaska Fairbanks, and Helix Systems Biowulf cluster at the National Institutes of Health, Bethesda, MD. S.E.M. was supported by the National Research Council.

- ¹G. E. Brown, Jr. *et al.*, *Chem. Rev.* **99**, 77 (1999).
- ²J. Wang, A. G. Kalinichev, and R. J. Kirkpatrick, *Geochim. Cosmochim. Acta* **70**, 562 (2006).
- ³V. A. Ranea, W. F. Schneider, and I. Carmichael, *Surf. Sci.* **602**, 268 (2008).
- ⁴P. Liu, T. Kendelewicz, G. E. Brown, Jr., E. J. Nelson, and S. A. Chambers, *Surf. Sci.* **417**, 53 (1998).
- ⁵B. Kasprzyk-Hordern, *Adv. Colloid Interface Sci.* **110**, 19 (2004).
- ⁶M. Henderson, *Surf. Sci. Rep.* **46**, 1 (2002).
- ⁷P. Fenter and N. C. Sturchio, *Prog. Surf. Sci.* **77**, 171 (2004).
- ⁸B. Braunschweig, S. Eissner, and W. Daum, *J. Phys. Chem. C* **112**, 1751 (2008).
- ⁹J. G. Catalano, P. Fenter, and C. Park, *Geochim. Cosmochim. Acta* **71**, 5313 (2007).
- ¹⁰X. G. Wang, W. Weiss, S. K. Shaikhutdinov, M. Ritter, M. Petersen, F. Wagner, R. Schlogl, and M. Scheffler, *Phys. Rev. Lett.* **81**, 1038 (1998).
- ¹¹A. Barbier, A. Stierle, F. Finocchi, and J. Jupille, *J. Phys.: Condens. Matter* **20**, 184014 (2008).
- ¹²J. A. Kelber, *Surf. Sci. Rep.* **62**, 271 (2007).
- ¹³P. J. Feibelman, *Phys. Today* **63**, 34 (2010).
- ¹⁴G. Waychunas, C. S. Kim, and J. F. Banfield, *J. Nanopart. Res.* **7**, 409 (2005).
- ¹⁵X. Xie, Y. Li, Z.-Q. Liu, M. Haruta, and W. Shen, *Nature (London)* **458**, 746 (2009).
- ¹⁶R. Gorte and J. Vohs, *Curr. Opin. Colloid Interface Sci.* **14**, 236 (2009).
- ¹⁷A. V. Whitney, J. W. Elam, S. L. Zou, A. V. Zinovev, P. C. Stair, G. C. Schatz, and R. P. Van Duyne, *J. Phys. Chem. B* **109**, 20522 (2005).
- ¹⁸C. Ruberto, Y. Yourdshahyan, and B. I. Lundqvist, *Phys. Rev. B* **67**, 195412 (2003).
- ¹⁹T. P. Trainor, P. J. Eng, G. E. Brown, Jr., I. K. Robinson, and M. D. Santis, *Surf. Sci.* **496**, 238 (2002).
- ²⁰W. J. Gignac, R. S. Williams, and S. P. Kowalczyk, *Phys. Rev. B* **32**, 1237 (1985).
- ²¹M. Gillet, A. Al Mohammad, K. Masek, and E. Gillet, *Thin Solid Films* **374**, 134 (2000).
- ²²M. Gautier, J. P. Duraud, L. P. Van, and M. J. Guittet, *Surf. Sci.* **250**, 71 (1991).
- ²³C. Verdozzi, D. R. Jennison, P. A. Schultz, and M. P. Sears, *Phys. Rev. Lett.* **82**, 799 (1999).
- ²⁴J. Guo, D. E. Ellis, and D. J. Lam, *Phys. Rev. B* **45**, 13647 (1992).
- ²⁵G. E. Brown, Jr., T. P. Trainor, and A. M. Chaka, in *Chemical Bonding at Surfaces and Interfaces*, edited by A. Nilsson, L. Pettersson, and J. Nørskov (Elsevier, Amsterdam, 2007), pp. 547–509.
- ²⁶P. J. Eng, T. P. Trainor, G. E. Brown, Jr., G. A. Waychunas, M. Newville, S. R. Sutton, and M. L. Rivers, *Science* **288**, 1029 (2000).
- ²⁷A. Thomas and H. Richardson, *J. Phys. Chem. C* **112**, 20033 (2008).
- ²⁸J. Toofan and P. R. Watson, *Surf. Sci.* **401**, 162 (1998).
- ²⁹K. C. Hass, W. F. Schneider, A. Curioni, and W. Andreoni, *Science* **282**, 265 (1998).
- ³⁰X.-G. Wang, A. Chaka, and M. Scheffler, *Phys. Rev. Lett.* **84**, 3650 (2000).
- ³¹Z. Łodziana, J. K. Nørskov, and P. Stoltze, *J. Chem. Phys.* **118**, 11179 (2003).
- ³²V. A. Ranea, I. Carmichael, and W. F. Schneider, *J. Phys. Chem. C* **113**, 2149 (2009).
- ³³J. R. Bargar, G. E. Brown, Jr., and G. A. Parks, *Geochim. Cosmochim. Acta* **61**, 2617 (1997).
- ³⁴J. G. Catalano, C. Park, Z. Zhang, and P. Fenter, *Langmuir* **22**, 4668 (2006).
- ³⁵T. Nguyen, D. Bonamy, L. Pham Van, L. Barbier, and J. Cousty, *Surf. Sci.* **602**, 3232 (2008).
- ³⁶K. S. Tanwar, C. S. Lo, P. J. Eng, J. G. Catalano, D. A. Walko, G. E. Brown, Jr., G. A. Waychunas, A. M. Chaka, and T. P. Trainor, *Surf. Sci.* **601**, 460 (2007).
- ³⁷C. S. Lo, K. S. Tanwar, A. M. Chaka, and T. P. Trainor, *Phys. Rev. B* **75**, 075425 (2007).
- ³⁸K. S. Tanwar, J. G. Catalano, S. C. Petitto, S. K. Ghose, P. J. Eng, and T. P. Trainor, *Surf. Sci. Lett.* **601**, L59 (2007).
- ³⁹K. Simeonov and D. Lederman, *Surf. Sci.* **603**, 232 (2009).
- ⁴⁰A. Marmier and S. C. Parker, *Phys. Rev. B* **69**, 115409 (2004).
- ⁴¹L. G. V. Briquet, C. R. A. Catlow, and A. A. French, *J. Phys. Chem. C* **113**, 16747 (2009).
- ⁴²J. P. Perdew, K. Burke, and M. Ernzerhof, *Phys. Rev. Lett.* **77**, 3865 (1996).
- ⁴³B. Delley, *J. Chem. Phys.* **92**, 508 (1990).
- ⁴⁴B. Delley, *J. Chem. Phys.* **113**, 7756 (2000).
- ⁴⁵Certain commercial software is identified in this paper to foster understanding.
- ⁴⁶H. J. Monkhorst and J. D. Pack, *Phys. Rev. B* **13**, 5188 (1976).
- ⁴⁷T. P. Trainor, A. M. Chaka, P. J. Eng, M. Newville, G. A. Waychunas, J. G. Catalano, and G. E. Brown, Jr., *Surf. Sci.* **573**, 204 (2004).
- ⁴⁸K. Reuter and M. Scheffler, *Phys. Rev. B* **65**, 035406 (2001).
- ⁴⁹*Crystal Structures* (Wiley, New York, 1964), Vol. 2.
- ⁵⁰R. Meyer, Q. Ge, J. Lockmeyer, R. Yeates, M. Lemanski, D. Reinalda, and M. Neurock, *Surf. Sci.* **601**, 134 (2007).
- ⁵¹B. Hinnemann and E. A. Carter, *J. Phys. Chem. C* **111**, 7105 (2007).

- ⁵²S. A. Prosandeev, E. Cockayne, B. P. Burton, S. Kamba, J. Petzelt, Y. Yuzyuk, R. S. Katiyar, and S. B. Vakhrushev, *Phys. Rev. B* **70**, 134110 (2004).
- ⁵³Q. Sun, K. Reuter, and M. Scheffler, *Phys. Rev. B* **67**, 205424 (2003).
- ⁵⁴K. Reuter and M. Scheffler, *Phys. Rev. B* **68**, 045407 (2003).
- ⁵⁵*NIST-JANAF Thermochemical Tables*, 4th ed., edited by J. Chase (American Chemical Society, Washington, DC, 1998).
- ⁵⁶*CRC Handbook of Chemistry and Physics*, 85th ed., edited by D. R. Lide (CRC Press, Boca Raton, FL, 2004).
- ⁵⁷A. Barbier, A. Stierle, N. Kasper, M.-J. Guittet, and J. Jupille, *Phys. Rev. B* **75**, 233406 (2007).
- ⁵⁸S. E. Mason, E. A. Sokol, V. R. Cooper, and A. M. Rappe, *J. Phys. Chem. A* **113**, 4134 (2009).
- ⁵⁹E. A. Jarvis and A. M. Chaka, *Surf. Sci.* **601**, 1909 (2007).
- ⁶⁰C. Lemire, S. Bertarione, A. Zecchina, D. Scarano, A. M. Chaka, S. Shaikhutdinov, and H.-J. Freund, *Phys. Rev. Lett.* **94**, 166101 (2005).
- ⁶¹B. D. Flockhart, J. A. N. Scott, and R. C. Pink, *Trans. Faraday Soc.* **62**, 730 (1966).
- ⁶²K. C. Hass, W. F. Schneider, A. Curioni, and W. Andreoni, *J. Phys. Chem. B* **104**, 5527 (2000).
- ⁶³S. E. Mason, C. R. Iceman, K. Tanwar, T. P. Trainor, and A. M. Chaka, *J. Phys. Chem. C* **113**, 2159 (2009).
- ⁶⁴Details of the α -Al₂O₃ (0001) calculations are reported in Ref. [63](#).
- ⁶⁵J.-H. Choi, D.-Y. Kim, B. Hockey, S. Wiederhotn, C. Handwerker, J. Blendell, W. Carter, and A. Roosen, *J. Am. Ceram. Soc.* **80**, 62 (1997).
- ⁶⁶T. Hiemstra, H. Yong, and W. Van Riemsdijk, *J. Colloid Interface Sci.* **184**, 680 (1996).